Tribology International 221 (2026) 112049

Contents lists available at ScienceDirect

Tribology International

journal homepage: www.elsevier.com/locate/triboint

Full Length Article

Lubrication film thickness prediction in the sliding contacts of axial piston pumps using physics-informed neural network

Hongsen Qiu, Lawrence Tinsley, Agusmian Partogi Ompusunggu *

Cranfield University, Faculty of Engineering and Applied Sciences (FEAS), College Road, Cranfield, MK43 0AL, Bedfordshire, UK

ARTICLE INFO

Keywords:
Physics-informed neural network (PINN)
Finite difference methods (FDM)
Oil film thickness
Axial piston pumps
Slipper pair

ABSTRACT

This paper presents the development of a novel Physics-Informed Neural Networks (PINN) method to predict lubrication film characteristics at the slipper–swashplate interface of axial piston pumps. It embeds the Reynolds equation and continuity conditions into the neural network's (NN) loss function, bridging conventional numerical simulations and data-driven methods. A numerical model for the slipper–swashplate interface was established using the Finite Difference Method (FDM) to generate datasets for training two PINN model variants that incorporate physical constraints, as well as a counterpart pure-data-driven Neural Network (NN) model. The validation shows excellent accuracy of the PINN models (the relative error below 5%) compared with the counterpart NN model (the relative error about 8%). Regarding prediction runtime, the trained PINN and NN models reduce computational time by 99.4% relative to the FDM approach. The study highlights the capabilities and limitations of PINN in tribology, stressing explicit geometric constraints for physical consistency. This study presents an efficient surrogate model for real-time lubrication assessment, establishes a framework for using PINNs in complex tribological systems, and contributes to hydraulic system design optimization and condition monitoring to enable more efficient operation of axial piston pumps.

1. Introduction

1.1. Background

Lubrication plays a fundamental role in mechanical systems, where thin oil films serve as critical interfaces that minimize wear, reduce friction, and enhance operational efficiency across various components, including bearings, engine pistons, gears, and slipper pairs in axial piston pumps. The effectiveness of these lubrication systems is particularly crucial in high-performance applications where reliability and efficiency are paramount.

Axial piston pumps represent a cornerstone technology in modern hydraulic systems, finding extensive applications across aerospace, naval vessel, rail transit, national defence, and military industries due to their superior power density, precise control capabilities, and robust performance characteristics [1–3]. These pumps rely heavily on stable oil films at the slipper–swashplate interfaces to effectively transfer high loads while minimizing internal leakage. The complex dynamics of these interfaces, operating under high-pressure and high-speed conditions, demand sophisticated lubrication analysis to ensure optimal performance and prevent catastrophic failures. Fig. 1 illustrates the typical configuration of an axial piston pump, consisting of a valve plate, a cylinder block, multiple pistons with slippers, a swash plate, and a drive shaft.

The lubrication film thickness plays a critical role in determining the working condition of the friction pair. For axial piston pumps, a lubrication film that is too thin can lead to excessive wear and even slipper burning damage due to insufficient separation and high surface temperature. On the other hand, if the oil film is too thick, it will reduce the sealing effect, increase internal leakage, and decrease the pump's volumetric efficiency [4–6]. Therefore, accurately predicting and analyzing oil film thickness is very important for designing and maintaining reliable machines. It helps engineers understand the lubrication status, improve performance, decrease wear and avoid failures [7]. However, the complex dynamics of slipper–swashplate interfaces, characterized by high-pressure, high-speed conditions and intricate geometric configurations, present significant challenges for traditional computational methods, necessitating the development of more efficient and accurate modeling approaches.

Traditionally, computational fluid dynamics (CFD) methods model lubrication by solving the Reynolds equation, by capturing fluid motion, elastic deformation, and pressure-viscosity effects. However, CFD simulations are computationally intensive and slow, particularly for

* Corresponding author.
E-mail address: agusmian.ompusunggu@cranfield.ac.uk (A.P. Ompusunggu).

https://doi.org/10.1016/j.triboint.2026.112049
Received 18 December 2025; Received in revised form 5 March 2026; Accepted 12 April 2026
Available online 14 April 2026
0301-679X/© 2026 The Author(s). Published by Elsevier Ltd. This is an open access article under the CC BY license (http://creativecommons.org/licenses/by/4.0/).

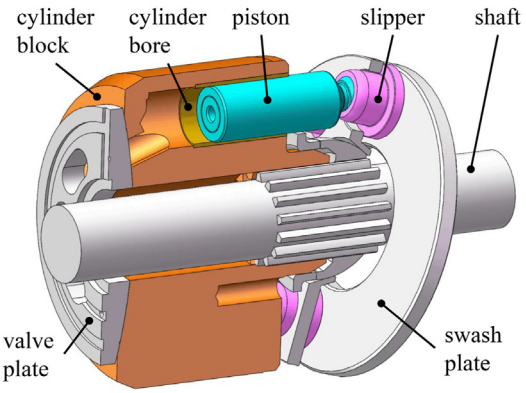

Fig. 1. General configuration of axial piston pump [9].

complex geometries and dynamic loading conditions. On the other hand, purely data-driven machine learning approaches offer computational speed and convenience but require extensive high-quality datasets and typically lack physical consistency and interpretability, limiting their reliability and generalization beyond the training data. To address these limitations, this study adopts the Physics-Informed Neural Networks (PINN) framework [8].

PINN are machine learning models that directly incorporate known physical laws, such as the Navier–Stokes equation, into neural network training. Rather than solely depending on large datasets, PINN embed these governing equations into their loss functions, ensuring predictions align closely with known physics. This enhances accuracy, interpretability, and reliability, even with limited data. In lubrication modeling, PINN present a promising, computationally efficient alternative to traditional CFD, accurately simulating lubrication films in sliding contacts, especially under complex and dynamic conditions.

1.2. Related works

PINN modeling framework is a transformative paradigm in scientific machine learning that combines data-driven approaches with the laws of physics. PINN is a class of deep learning neural networks that can learn the response of physical systems without requiring large amounts of simulation data by embedding the partial differential equations (PDEs) or ordinary differential equations (ODEs) of physical systems into their loss functions. The concept of PINN was significantly advanced by Raissi et al. [8]. The core idea is to approximate the PDE solution using a fully connected neural network and compute the derivatives through automatic differentiation (AD). Training involves minimizing a combined loss function that includes the PDE residual, initial conditions, and boundary conditions, transforming the PDE solution into an unconstrained optimization problem. The meshless nature of PINN allows them to handle complex or high-dimensional geometries. This approach provides a more robust, interpretable, and generalizable modeling approach for data-scarce applications by incorporating the laws of physics into the loss function [10].

The development of PINN stems from the progress of deep neural networks and aims to bridge the gap between machine learning and scientific computing [11]. Traditional numerical methods (such as finite elements) are computationally expensive and require specific adjustments [12], while purely data-driven models face the problems of data scarcity and insufficient generalization ability [13]. PINN exploit the ability of neural networks to solve differential equations while obeying the laws of physics, aiming to provide more efficient and flexible solvers to handle complex physical systems such as nonlinearities or shock waves. Its core motivation is to address the challenges of data scarcity and physical plausibility in scientific engineering, and ensure the accuracy and physical consistency of model results by incorporating physical laws into the learning process [14,15]. The laws of physics serve as a powerful form of regularization, allowing PINN to achieve accurate and generalizable solutions even with limited data, making them attractive in applications where data acquisition is expensive and physical consistency is critical.

The ideal entry point for applying PINN in tribology is the Reynolds equation, the governing PDE for hydrodynamic lubrication. It describes the pressure distribution in thin, viscous fluid films under assumptions of laminar, iso-viscous, and incompressible flow, forming the bedrock of lubrication analysis.

The PINN formulation for this problem begins with a standard feedforward neural network, or multilayer perceptron (MLP), which is structured to approximate the pressure field, $p(x, y; \theta)$ and thickness field $h(x, y; \theta)$, where θ represents the network's trainable weights and biases. The network takes spatial coordinates (x, y) as input and yields the predicted pressure as output. The core of the method is a composite loss function that the network is trained to minimize.

Pioneering studies in tribology have validated this approach. Among others, Almqvist et al. [16] provided a foundational, fully explicit mathematical description of a PINN for the one-dimensional Reynolds boundary value problem, demonstrating its feasibility and accuracy against analytical solutions. This was followed by the work of Zhao et al. [17], who extended the method to the two-dimensional Reynolds equation. They validated the PINN predictions for pressure distribution and film thickness against both FEM simulations and experimental results, achieving strong agreement. These early successes firmly established PINN as a legitimate, meshless computational tool for hydrodynamic lubrication, opening the door to tackling more complex tribological phenomena.

Li et al. [18] compared the application of three deep learning strategies, supervised, unsupervised, and semi-supervised, in solving the Reynolds equation for gas bearings. The study revealed a trade-off between prediction accuracy and physical interpretability, and pointed out that semi-supervised learning can achieve the best balance between the two with a small amount of data, making it a practical solution.

Xi et al. [19] applied PINN to solve the Reynolds equations for journal bearings, focusing on comparing soft and hard constraint methods for applying boundary conditions. The study found that applying hard constraints by constructing specific functions can significantly improve the accuracy of boundary value solutions. Rom [20] first applied PINN to complex Reynolds equations involving cavitation models. The proposed "extended PINN" model incorporates physical parameters as network inputs, enabling a single model to solve for multiple operating conditions, thereby creating a general surrogate model capable of rapid and accurate predictions, with significant potential for parameterization studies and optimization design. Cheng et al. [21] developed the HL-nets framework, systematically comparing two approaches for handling inequalities and complementary constraints in cavitation models. The study clearly demonstrated that the method of "imposing" constraints by altering the network structure significantly outperforms the traditional "penalization function" method in terms of computational accuracy and stability.

Huang et al. [22] reviewed the design challenges for slipper pairs in high-pressure axial piston pumps, emphasizing the limitations of traditional PV value-based methods for high-pressure applications. The study concludes that a comprehensive understanding of micro-scale oil film dynamics and fluid–structure coupling is essential for optimizing the slipper structure to prevent friction and wear failures at pressures exceeding 42 MPa. Ransegnola et al. [23] developed a strongly coupled simulation model to investigate the mutual interaction between lubricating interfaces and its effect on the spin dynamics of the piston and slipper in axial piston machines. The study revealed that piston spin is highly dependent on operating conditions, especially the swashplate angle, and that accurately modeling this spin is critical for predicting the machine's frictional losses and overall efficiency. Du et al. [24] developed a predictive method for the eccentric wear of slipper pairs by

establishing a mixed lubrication model that incorporates both abrasive and adhesive wear mechanisms. The research demonstrated that wear depth is primarily influenced by operating pressure and speed, and that the resulting wedge-shaped wear profile on the slipper's outer edge can paradoxically enhance the hydrodynamic effect, thereby improving lubrication performance. Zhao et al. [25] conducted a numerical and experimental analysis of fluid dynamic lubrication for slippers with various surface structures (single, double, and four-support belts) in valve distribution piston pumps. The results showed that while multi-support belt structures can reduce friction torque by up to 17.07%, they also increase the probability of slipper overturning, revealing a design conflict between reducing friction and ensuring stability. Ye et al. [26] developed a new coupled dynamic model to simultaneously analyze the dynamic vibrations of the slipper and piston and the lubrication characteristics of the oil film at the slipper/swash-plate interface. The study concluded that the vibration responses and oil film thickness are strongly interdependent, with the relative motions between components influencing the oil film and the film's nonlinear properties affecting the bodies' vibration behavior.

1.3. Research gaps

To the best of the authors' knowledge, we have not found any published works that developed a PINN model to estimate the film thickness in the slipper pair of axial piston pumps. A significant research gap exists at the intersection of these two fields. While PINN have been validated on lubrication problems with prescribed geometries and boundary conditions, its application to a fully coupled, multi-degree-of-freedom dynamic system like the slipper pair, where the oil film thickness and boundary pressures are themselves unknown outputs of the system's dynamic equilibrium, remains unexplored. This gap is critical because traditional dynamic simulations, while detailed, are too computationally expensive for rapid parameter studies, optimization tasks, or potential real-time control applications.

1.4. Aim, objectives and main contributions

To address the research gaps formulated in the previous subsection, the primary aim of this paper is to enhance the prediction efficiency of lubrication film thickness and pressure field in sliding contact systems by developing a PINN surrogate model. This approach seeks to minimize the time required for simulations while maintaining an acceptable level of predictive accuracy. To achieve the aim, physical governing equations for axial piston pumps will be embedded into a neural network architecture.

The main contributions of this work are highlighted as follows.

- To construct and train a PINN that incorporates the Reynolds and continuity equations for modeling lubrication film status.
- To develop a CFD-based numerical simulation of lubrication flow in sliding contact configurations and generate a dataset for training and validating the PINN model.
- To benchmark the predictive accuracy and computational efficiency of the developed PINN model against conventional CFD simulations.
- To evaluate the generalization capability of the PINN model under various operating and loading conditions.

1.5. Paper organization

The remainder of this paper is structured as follows. Section 2 establishes the comprehensive methodological framework for this study. It begins by detailing the high-fidelity tribo-dynamic numerical model, which integrates rigid-body kinematics with the Reynolds equation to generate the ground-truth dataset for training. Subsequently, the architecture of the PINN is presented, with a specific focus on the evolution from a standard soft-constrained model (PINN-1) to an enhanced architecture incorporating hard geometric constraints (PINN-2). Section 3 provides a critical analysis of the results. It starts with an examination of the flow field characteristics derived from the CFD simulations, followed by a rigorous benchmarking of the PINN' predictive performance against the numerical baseline. This section evaluates the models in terms of transient tracking accuracy, spatial field distribution, error metrics, and computational efficiency. Finally, Section 4 summarizes the key findings of this research and outlines potential directions for future work in extending PINN to complex tribological systems.

2. Methodology

This chapter details the methodological framework for predicting the lubrication characteristics of an axial piston pump's slipper pair. The approach is twofold. First, a high-fidelity numerical model is established, incorporating kinematic analysis and the governing Reynolds equation, which serves as the source for generating training and validation datasets. Second, the architecture and training process of a PINN are defined. The core of this method is the formulation of a composite loss function that embeds the governing physical laws as soft constraints. This ensures the network's predictions are not only data-driven but also physically consistent across the entire domain, creating a computationally efficient surrogate model.

2.1. Slipper pair tribo-dynamic model for data generation

This section presents the comprehensive mathematical model describing the tribo-dynamic behavior of the slipper pair. This high-fidelity numerical model serves two primary purposes: (1) to fundamentally analyze the complex interplay between the slipper's motion and the lubricating oil film's characteristics; (2) to generate the extensive dataset required for the subsequent training and validation of the PINN surrogate model. The model development integrates the slipper's multi-degree-of-freedom (DOF) dynamics with the governing equations of hydrodynamic lubrication.

2.1.1. Slipper dynamic model

To model the complex motion of the slipper, as shown in Fig. 2, three coordinate systems are established. They serve as foundational references for the FDM formulation, as they define the global/local coordinate systems, variable directions, and geometric relations used throughout the governing equations. A global stationary coordinate system ($O-XYZ$) is fixed to the pump housing, followed by a rotating frame ($O-X'Y'Z'$) that revolves with the cylinder block to describe the orbital motion of the slipper assembly. Finally, a local, body-fixed coordinate system ($O_s-X_sY_sZ_s$) is attached to the slipper to define its own dynamic behavior, particularly its axial displacement and tilting angles. The kinematic transformations between these frames allow for a complete description of the slipper's position and orientation relative to the swashplate.

The intricate motion of the slipper relative to the swashplate is simplified to three principal degrees of freedom (DOF), which are sufficient to capture its essential dynamic behavior: axial translation along its central axis (z_s), and tilting rotations about the two orthogonal axes (x_s and y_s) in its own body-fixed coordinate system. The dynamic equilibrium of the slipper is governed by Newton's second law, which can be expressed in a generalized matrix form as:

$$\mathbf{M}\ddot{\mathbf{q}} + \mathbf{C}\dot{\mathbf{q}} + \mathbf{K}\mathbf{q} = \mathbf{Q} \tag{1}$$

where $\mathbf{q}$, $\dot{\mathbf{q}}$, and $\ddot{\mathbf{q}}$ are the generalized vectors for displacement, velocity, and acceleration, respectively, defined as $q = \{z_s, \alpha, \beta\}^T$. The terms $\mathbf{M}$, $\mathbf{C}$, and $\mathbf{K}$ represent the generalized mass, damping, and stiffness matrices of the slipper assembly. Fig. 3 shows the specific location of the coefficient of damping and stiffness at the spherical joint.

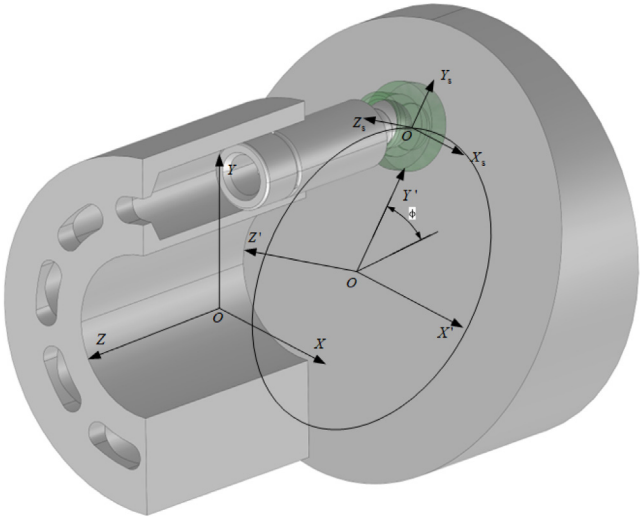

Fig. 2. Coordinate system for slipper dynamics.

The vector **Q** on the right-hand side represents the sum of all external generalized forces and moments acting on the slipper. It is conceptually divided into two main components:

$$\mathbf{Q} = \mathbf{Q_{ext}} + \mathbf{Q_{oil}} \tag{2}$$

Here, $\mathbf{Q_{ext}}$ encompasses forces arising from the piston chamber pressure and inertial effects. The primary axial force component results from the high-pressure fluid acting on the piston area, which can be expressed as $Fz = -\pi R_p^2 p_w cos\beta$ (see the derivation in Appendix A.1), where p_w is the instantaneous piston chamber pressure, R_p is the piston radius, and β is the swashplate angle. Additional moment components in $\mathbf{Q_{ext}}$ are generated by centrifugal forces and inertial effects due to the slipper's orbital motion around the pump's main axis.

The term $\mathbf{Q_{oil}}$ represents the reaction forces and moments generated by the lubricating oil film. These are obtained by integrating the pressure distribution $p(r,\theta)$ over the slipper's sealing land area (A):

$$\mathbf{Q_{oil}} = \{F_r, M_{rx}, M_{ry}\} \tag{3}$$

$$\begin{cases} F_r = \int_0^{2\pi}\int_{R_1}^{R_2} p(r,\theta) dA \\ M_{rx} = \int_0^{2\pi}\int_{R_1}^{R_2} p(r,\theta) r cos\theta dA \\ M_{ry} = \int_0^{2\pi}\int_{R_1}^{R_2} -p(r,\theta) r sin\theta dA \end{cases} \tag{4}$$

This force vector creates a direct coupling between the slipper's dynamic motion and the oil film's pressure field, making the entire system a tightly coupled, nonlinear problem.

2.1.2. Lubrication film model

The performance of the slipper–swashplate interface is fundamentally dictated by the thin oil film separating the two surfaces. The model for this film is defined by its thickness profile and the pressure distribution within it. The local thickness of the oil film, h, at any point (r,θ) on the slipper sealing land is a function of the slipper's instantaneous dynamic state. It is geometrically defined as the sum of the central film thickness, h_c, and the variations caused by the slipper's tilting angles, α and β (see the derivation in Appendix A.2):

$$h(r,\theta,t) = h_c(t) + \alpha(t) r \sin\theta + \beta(t) r \cos\theta. \tag{5}$$

The central thickness h_c is directly related to the axial displacement z_s. This equation links the slipper's dynamics directly to the geometry of the lubrication gap, which in turn governs the pressure generation.

Meanwhile, the pressure distribution $p(r,\theta,t)$ within the oil film is governed by the two-dimensional Reynolds equation [27], expressed here in cylindrical coordinates to match the slipper's geometry:

$$\frac{\partial}{\partial r}\left(\frac{rh^3}{12\mu}\frac{\partial p}{\partial r}\right) + \frac{1}{r}\frac{\partial}{\partial \theta}\left(\frac{h^3}{12\mu}\frac{\partial p}{\partial \theta}\right) = \frac{1}{2}\frac{\partial}{\partial r}(rhU_r) + \frac{1}{2}\frac{\partial}{\partial \theta}(hU_\theta) + \frac{\partial h}{\partial t} \tag{6}$$

where μ is the dynamic viscosity of the lubricant. The terms on the right-hand side represent the physical mechanisms of pressure generation. The first two terms, involving the relative tangential (U_θ) and radial (U_r) velocities, describe the hydrodynamic wedge effect caused by the slipper's orbital motion and tilting. The final term, $\partial h/\partial t$, represents the squeeze effect, which generates pressure due to the time-varying film thickness.

To obtain a unique solution for the pressure field, the Reynolds equation must be supplemented with a set of appropriate boundary conditions:

1. Pressure Boundaries: The pressure at the outer radius of the slipper sealing land ($r = R_2$) is set to the casing pressure (typically atmospheric). The pressure at the inner radius ($r = R_1$) is determined by the pressure in the slipper's central pocket, p_{in}.
2. Flow Continuity: The pressure p_{in} is not constant; it is determined by the balance between the oil flowing into the pocket from the piston chamber through a throttle orifice and the oil leaking out across the inner sealing land. This mass conservation principle yields a continuity equation: $Q_{in} = Q_{out}$. The inflow is modeled as follow:

   $$Q_{in} = (p_w - p_{in})/C_t. \tag{7}$$

   where C_t is the flow resistance of the throttle. The outflow, Q_{out}, is calculated by integrating the radial flow rate at the outer boundary ($r = R_2$). Which can be expressed as:

   $$Q_{out} = \int_0^{2\pi} \frac{h^3}{12\mu}\frac{\partial p}{\partial r} r d\theta. \tag{8}$$

3. Periodicity: Due to the circular geometry, the pressure and its gradient must be continuous in the circumferential direction, such that $p(r,0) = p(r,2\pi)$ and $(\partial p/\partial\theta)|_{\theta=0} = (\partial p/\partial\theta)|_{\theta=2\pi}$.

2.1.3. Numerical solution framework

The tribo-dynamic model constitutes a system of coupled, nonlinear differential equations. The slipper's dynamic equations of motion are ordinary differential equations (ODEs) in time, while the Reynolds equation is a partial differential equation (PDE) over the spatial domain of the oil film. A robust numerical scheme is required to solve this system.

Fig. 4 shows the overall simulation work flow for solving the dynamic model of oil film of slipper pair. The solution is advanced in time using a step-by-step integration method. At each time step, an iterative procedure is employed to ensure convergence between the slipper dynamics and the lubrication model. First, the Reynolds equation is discretized on a polar grid using a second-order accurate finite difference method (FDM). The resulting large, sparse system of linear algebraic equations for the nodal pressures is then solved efficiently using an iterative solver like the Successive Over-Relaxation (SOR) method [28]. Once the pressure field converges, the film reaction force Q_{oil} is calculated via numerical integration. This force is then substituted back into the slipper's dynamic equations, which are solved to update the slipper's position and velocity $(q, \dot{q})$ for the next time step.

This simulation framework is executed across a wide range of predefined operating conditions (i.e., varying pump speeds and delivery pressures) to systematically generate a comprehensive database. This database, containing the instantaneous slipper states and the corresponding oil film pressure and thickness fields, forms the ground truth for training and rigorously testing the PINN-based surrogate model detailed in Section 2.3.

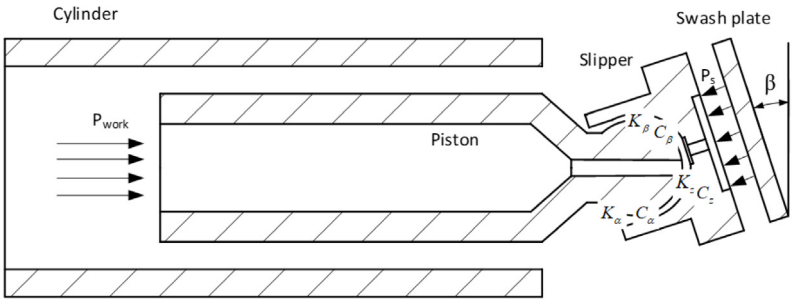

Fig. 3. Schematic of damping coefficient at spherical joint.

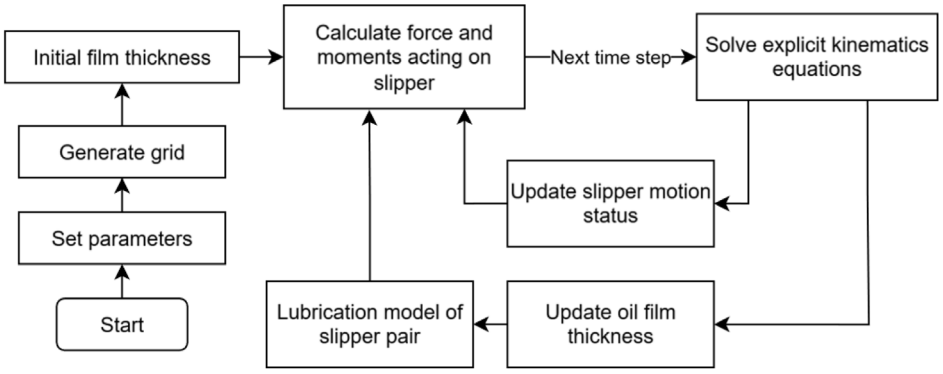

Fig. 4. Flowchart for solving the oil film of slipper pair.

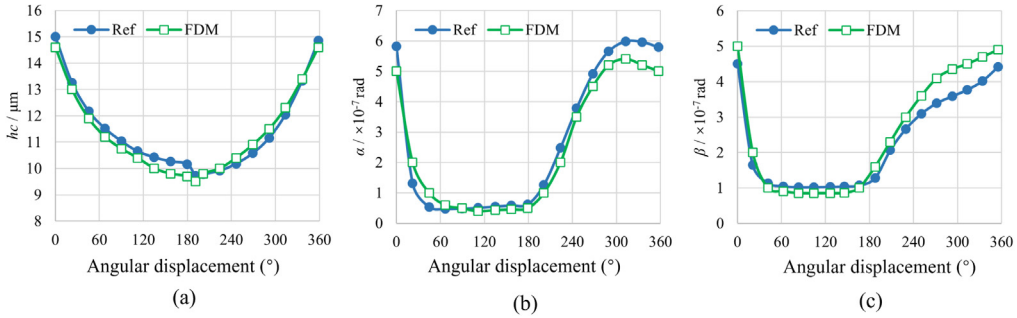

Fig. 5. Comparison between the present FDM simulation and reference results [17]: (a) central film thickness h_c, (b) tilting angle α, and (c) tilting angle β as functions of angular displacement.

2.2. Validation of the FDM model

To verify the accuracy and reliability of the proposed Finite Difference Method (FDM) numerical framework, the simulation results are compared against benchmark data from established literature [17]. The validation focuses on the transient kinematic characteristics of the slipper–swashplate sliding contact over a complete shaft revolution (0° to 360°). Specifically, the comparisons are evaluated based on three critical dynamic parameters: the central film thickness (h_c), the tilt angle in the x-direction (α), and the tilt angle in the y-direction (β).

Fig. 5 illustrates the comparative analysis between the proposed FDM model and the reference data. As depicted in Fig. 5(a), the predicted central oil film thickness h_c exhibits a strong correlation with the literature results, accurately capturing the periodic dynamic fluctuations induced by the fluctuating operating pressure throughout the pump cycle. Furthermore, the simulated tilt angles α and β, presented in Fig. 5(b) and Fig. 5(c) respectively, align closely with the benchmark data in terms of both phase and amplitude. The numerical model successfully reproduces the complex, coupled multi-axial tilting behaviors of the slipper under transient elastohydrodynamic conditions.

Although minor discrepancies can be observed at certain peak values and transitional phases—which are primarily attributable to variations in spatial discretization density, specific convergence tolerances, or slight differences in the numerical treatment of the boundary conditions—the overall dynamic trends remain highly consistent. This rigorous agreement comprehensively demonstrates the validity and effectiveness of the proposed FDM solver. Consequently, the established FDM framework is proven to be robust and accurate, serving as a highly credible ground-truth baseline for the subsequent development, training, and evaluation of the Physics-Informed Neural Network (PINN) model.

2.3. Lubrication prediction based on PINN

PINN is an emerging modeling approach that integrates physical laws with deep learning techniques. Unlike traditional numerical methods, PINN not only leverage observational data for training but also embed governing equations and boundary conditions directly into the loss function of the neural network, thereby enhancing the model's

generalization ability and physical consistency. This approach is particularly advantageous for solving complex physical field problems, as it reduces the reliance on large labeled datasets and offers strong nonlinear fitting capabilities.

In slipper pair oil film lubrication, accurate prediction of the oil film pressure distribution is crucial for lubrication performance analysis and structural optimization. By employing PINN, it is possible to efficiently predict the oil film pressure field with limited data while strictly adhering to physical constraints. PINN can automatically satisfy governing equations such as the Reynolds equation and flexibly handle boundary and continuity conditions, making them suitable for complex geometries and multi-physics coupling problems.

This section introduces the PINN-based lubrication prediction method. First, the basic structure and the modeling process of PINN are described. Subsequently, the construction of the physics loss, the training procedure, and the specific application of PINN to the slipper pair oil film lubrication problem are detailed, laying the foundation for the subsequent discussion of results. In this study, the full-cycle coupled behavior is learned from labels generated by the validated FDM dynamic framework; the dynamic influence is therefore learned implicitly from data labels rather than enforced by an explicit dynamics residual term in the PINN loss.

2.3.1. PINN structure

In this study, a Multi-Layer Perceptron (MLP) serves as the backbone architecture for the PINN. The Universal Approximation Theorem [29] ensures MLP's capability to represent the continuous pressure field $p(r,\theta)$ governed by the Reynolds equation. PINN utilize automatic differentiation to compute exact derivatives (e.g., $\partial p/\partial r$, $\partial^2 p/\partial\theta^2$) essential for physics-based loss functions, avoiding numerical errors from finite difference schemes. The MLP's structural simplicity and suitability for mapping low-dimensional coordinates (r,θ) to scalar pressure values p make it more appropriate than CNNs or RNNs for this application.

Fig. 6 illustrates the architecture of the initial model, PINN-1, which is based on the standard unsupervised approach. The network takes the polar coordinates (r,θ), angular displacement of piston φ and the working conditions (P_{work},ω) as input. The output layer directly yields the predicted pressure p and the film thickness h as scalar fields.

In the present formulation, the network input uses the angular displacement φ as the temporal coordinate, instead of using time t directly. For a given operating angular speed ω (in rad/s), we use the kinematic relation

$$\omega = \frac{d\varphi}{dt}, \qquad \varphi = \int_0^t \omega\, dt. \tag{9}$$

Therefore, the time derivative of the film thickness required in the Reynolds-equation residual is obtained through the chain rule:

$$\frac{\partial h}{\partial t} = \frac{\partial h}{\partial \varphi}\frac{\partial \varphi}{\partial t} = \omega\frac{\partial h}{\partial \varphi}. \tag{10}$$

This transformation is applied consistently when evaluating physics-loss terms, so that the model remains physically consistent while using φ-based inputs.

The total loss function, $\mathcal{L}_{\text{total}}$, is composed of the data loss ($\mathcal{L}_{\text{data}}$) and the physics loss ($\mathcal{L}_{\text{p}}$), which includes the Reynolds Equation Loss, Boundary Conditions Loss, and Continuity Loss. However, initial results from PINN-1 revealed that while the average film thickness was accurately predicted, the point-wise thickness distribution failed to strictly adhere to the geometric law of a planar surface. This physical inconsistency, attributed to the lack of an explicit geometric constraint, demonstrated that the network struggled to intrinsically learn the rigid-body kinematic relationship governing the film thickness.

To address this deficiency, an enhanced architecture, PINN-2, was developed, as shown in Fig. 7. The fundamental difference lies in how the film thickness is predicted, moving from a fully data-driven output to a Physics-Informed Parametric Output. In PINN-2, the output layer of the MLP is structurally modified to predict the pressure p alongside the three kinematic parameters that uniquely define the planar film profile: thickness at three monitoring points (h_1,h_2,h_3). These thickness values are used to calculate the spatial state of the oil film (h_c,α,β). Crucially, the final film thickness $h(r,\theta)$ is not directly predicted by the network, but is mathematically constructed in a subsequent layer using the geometric constraint established in Eq. (5). This architectural change effectively embeds the geometric constraint of the slipper pair's rigid-body motion directly into the forward pass of the network, acting as a hard constraint. This ensures that the predicted film thickness field h is mathematically guaranteed to be planar at all times, thereby enforcing physical consistency and dramatically improving the accuracy and interpretability of the results, as evidenced by the high physical accuracy achieved by PINN-2 compared to PINN-1.

Before inputting the dataset into the neural network for training, it is essential to sample and normalize the data. The raw data obtained through simulation calculations is extremely large, often containing redundant data, and the data scales of each dimension vary significantly. This can lead to issues such as gradient explosion or gradient vanishing during training, thereby affecting training efficiency.

In order to obtain important grid points of raw data, the grid points are divided into boundary points and internal points. Perform uniform sampling on these two sets of grid points separately to ensure there are sufficient boundary points. In this paper, the Z-score normalization method [30] is used to process data. The data is normalized according to the formula describe below:

$$x_{normal} = \frac{x-\sigma_d}{\mu_d}. \tag{11}$$

where σ_d is the standard deviation of raw data, μ_d is the mean of raw data. After that, the raw data is converted into a dataset with a mean of 0 and a standard deviation of 1.

For PINN, the loss function includes supervised points which are solutions from oil film simulation, and lubrication-physical losses, which involves Reynolds equation loss, boundary loss and continuity loss. The physics loss in this work is limited to lubrication-governing constraints (Reynolds equation, boundary conditions, continuity, and geometric constraints). The slipper dynamic equation is not explicitly embedded as a residual term. The total loss function is expressed as:

$$\mathcal{L}_{\text{total}} = \lambda_1\mathcal{L}_{\text{data}} + \lambda_2\mathcal{L}_{\text{Re}} + \lambda_3\mathcal{L}_{\text{bc}} + \lambda_4\mathcal{L}_{\text{c}}, \tag{12}$$

where $\lambda_1,\lambda_2,\lambda_3$ and λ_4 are weight coefficients of each loss term that determine the importance of each condition when updating PINN parameters.

The mean square error (MSE) is adopted to measure the loss of a neural network, and it can be expressed as follows:

$$\mathcal{L}_{\text{data}} = MSE = \frac{1}{N_d}\sum_{i=1}^{N_d}(\hat{y}(x_i)-y_i)^2. \tag{13}$$

where $\hat{y}(x_i)$ are predicted values, y_i are value of the input dataset, which are considered as true values.

The Reynolds equation is the main physical loss for the PINN model; it ensures that PINN's predicted values comply with the physical laws of oil film flow. To ensure consistency with physical laws, the Reynolds equation in the same form as in Section 2.1.2 is used. The Reynolds equation loss function can be defined as:

$$\mathcal{L}_{\text{Reynolds}} = \frac{1}{N_d}\sum_{i=1}^{N_d}\Big[\frac{\partial}{\partial r}\left(\frac{r_i h_i^3}{12\mu}\frac{\partial p_i}{\partial r}\right) + \frac{1}{r_i}\frac{\partial}{\partial\theta}\left(\frac{h_i^3}{12\mu}\frac{\partial p_i}{\partial\theta}\right) - \frac{1}{2}\frac{\partial}{\partial r}(r_i h_i U_{ir}) - \frac{1}{2}\frac{\partial}{\partial\theta}(h_i U_{i\theta}) - \frac{\partial h_i}{\partial t}\Big]^2. \tag{14}$$

To calculate the Reynolds equation loss correctly, predicted data $\hat{y}(p,h)$ are denormalized to the physical scale. This is because the input data of PINN are normalized before entering the model, and the output data from the model are also normalized. The derivative term of output $\hat{y}(p,h)$ also needs to be denormalized to the physical scale before calculating the Reynolds equation loss.

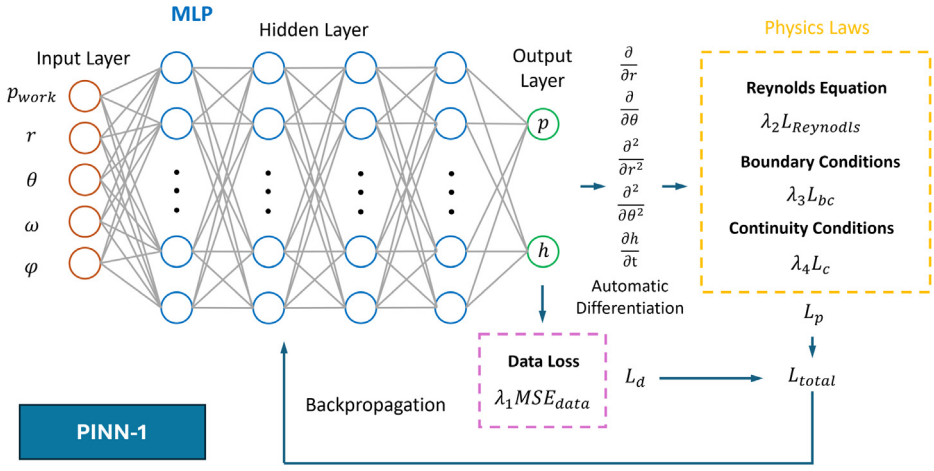

Fig. 6. The network structure of PINN-1.

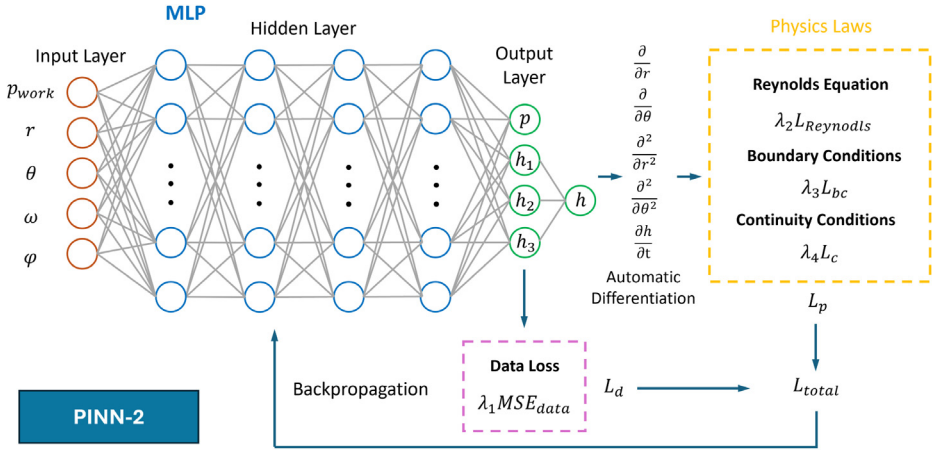

Fig. 7. The network structure of PINN-2.

Boundary loss constrains the physical condition of the boundary area in the physical domain. It is the inlet pressure at the inner boundary and the outlet pressure at the outer boundary, which is defined as:

$$\mathcal{L}_{\mathrm{bc}} = \frac{1}{N_d}\sum_{i=1}^{N_d}[\hat{p}_b(x_i) - p_b(x_i)]^2, \tag{15}$$

where, x_i is the input data of boundary domain, $\hat{p}_b$ is predicted boundary pressure. Note that p_b is the true boundary pressure, which is considered as 0 at the outlet and p_{in} at the inlet.

The loss of continuity conditions constrains the consistency of the inlet flow rate and outlet flow rate under the prediction values of the model, which is defined as:

$$\mathcal{L}_{\mathrm{c}} = \frac{1}{N_d}\sum_{i=1}^{N_d}[\hat{q}_{in}(x_i) - \hat{q}_{out}(x_i)]^2. \tag{16}$$

where $\hat{q}_{in}$ and $\hat{q}_{out}$ are predicted inlet flow rate and outlet flow rate, respectively. They are calculated by Eq. (7) and Eq. (8). This loss function ensures that the PINN model adheres to the mass conservation principle, which is crucial for accurately modeling the lubrication flow.

2.3.2. Dataset construction and training–testing split

To ensure a rigorous and unbiased evaluation of the proposed models, the dataset generated from the FDM simulations was systematically divided into training and testing subsets based on operating conditions rather than random sampling. Because the dataset is produced by a coupled FDM dynamic simulation, dynamic effects are embedded in the supervisory labels used to train the surrogate model.

The full simulation campaign covered four working pressures (10, 20, 30, and 40 MPa) and five rotational speeds (5,000, 10,000, 15,000, 20,000, and 25,000 RPM), yielding 20 baseline operating conditions. In addition, two supplementary in-domain operating conditions (20 MPa and 11,250 RPM) and (25 MPa and 12,500 RPM) were generated for the sensitivity analysis (see Section 3.2.4), resulting in a total of 22 operating conditions. For each condition, a complete operating cycle was simulated, and the corresponding pressure and film-thickness fields were recorded to form the dataset. For models testing and evaluation, the four operating conditions, namely (20 MPa and 15,000 RPM), (30 MPa and 20,000 RPM) and the two supplementary conditions were excluded from the training as unseen test conditions.

These two cases represent intermediate-high operating regimes and were selected to evaluate the interpolation and robustness performance of the trained models under unseen conditions. All remaining 18 operating conditions were used for training. This condition-based splitting strategy ensures that the testing data are physically independent from the training data, thereby preventing data leakage across operating regimes. Consequently, the reported prediction accuracy reflects the true generalization capability of the models across varying pressure–speed combinations rather than memorization of specific simulation states.

Table 1
Architecture and activation candidate comparison for hyperparameter determination.

Case	MLP structure	Activation	Final normalized total loss
A	[5,16,32,16,2]	ReLU	1.00
B	[5,16,64,16,2]	ReLU	0.73
C	[5,16,64,64,16,2]	ReLU	0.62
D	[5,16,64,16,2]	tanh	0.56
E (selected)	[5,16,64,64,16,2]	tanh	0.41
F	[5,16,96,96,16,2]	tanh	0.39

2.3.3. Methodology for loss-weight determination

The loss-term weights were determined through a validation-driven two-stage procedure. In the first stage, a broad logarithmic screening was conducted to identify suitable orders of magnitude for each coefficient. Candidate settings that led to unstable optimization or physically inconsistent predictions were discarded. In the second stage, local refinement was performed around promising regions using smaller multiplicative adjustments, with repeated training/evaluation cycles until no consistent improvement was observed.

The final configuration was selected by jointly considering prediction quality and physical consistency, rather than optimizing a single objective. In practice, this means balancing field-level prediction behavior with the satisfaction of governing-equation, boundary-condition, and continuity constraints. This multi-criteria strategy avoids over-fitting to one loss component and yields a more reliable overall model.

To reduce stochastic bias, shortlisted configurations were additionally checked under repeated runs with different random initializations and shuffled mini-batches. The selected setting showed stable convergence behavior and consistent physical plausibility across runs.

2.3.4. Hyperparameter determination for architecture and optimization

To improve reproducibility, we explicitly describe how architecture and optimization hyperparameters were selected. The screened items include MLP depth/width, activation function, batch size, and learning-rate strategy. A compact comparison of representative architecture–activation candidates is summarized in Table 1. Although Case F achieves a slightly lower loss, it uses a more complex network, which requires longer training and higher execution cost; therefore, Case E is selected as the final configuration due to its better overall complexity–efficiency trade-off.

The selection follows a two-stage procedure. First, a coarse screening is performed to identify feasible model complexity and activation candidates with stable optimization behavior. Second, local refinement is conducted around the best-performing region to obtain a configuration that balances convergence quality, physical consistency, and computational efficiency.

For optimization, a three-stage learning-rate schedule is adopted to accelerate convergence:

$$\eta = \begin{cases} 10^{-2}, & 0\%\text{–}25\% \text{ epochs}, \\ 10^{-3}, & 25\%\text{–}75\% \text{ epochs}, \\ 10^{-4}, & 75\%\text{–}100\% \text{ epochs}. \end{cases} \tag{17}$$

This staged strategy enables rapid descent in the early phase, stable transition in the middle phase, and fine optimization in the final phase, thereby improving overall convergence speed compared with using a single fixed learning rate.

Regarding mini-batch configuration, the selected batch size is chosen based on training throughput and optimization efficiency under the current hardware/software setting. In our implementation, this setting provides the fastest practical training speed while maintaining stable gradient updates for the coupled data/physics objectives.

For the activation function choice, tanh is preferred over ReLU-type alternatives in this task. The PINN requires smooth derivatives for automatic differentiation in PDE-related terms; tanh provides smoother first- and higher-order derivative behavior, thereby reducing non-physical oscillations and improving optimization stability in high-gradient transient regions. By contrast, piecewise-linear activations are more prone to derivative discontinuity effects in PDE-constrained training, which can degrade physical-field smoothness.

Based on the above protocol, the final model uses the selected MLP architecture, `tanh` activation, the chosen batch size, and the three-stage learning-rate schedule. All comparative results in Section 3 are reported under this fixed configuration for fair evaluation.

Table 2
Structural and operating parameters of slipper pair.

Parameters	Value
Inner radius R_1 (mm)	1.8
Outer radius R_2 (mm)	3.4
Piston diameter R_p (mm)	2.5
Slipper rotation radius R_c (mm)	10
Swashplate angle β (°)	18
Viscosity μ (Pa · s)	0.005
Atmospheric pressure p_{atm} (MPa)	0

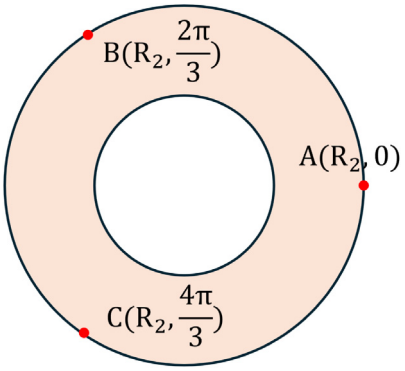

Fig. 8. Physical locations of three points for defining oil film plane.

3. Results and discussion

3.1. Oil film FDM simulation analysis

To ensure that simulations can provide comprehensive training and test datasets, it is essential to define a rational range and number of working conditions for the simulations. In order to ensure relatively stable simulation data, the simulation time was set to two operating cycles. The working condition parameters setting included working pressure and operating speed are set as (10 MPa, 20 MPa, 30 MPa, 40 MPa) and (5,000 RPM, 10,000 RPM, 15,000 RPM, 20,000 RPM, 25,000 RPM), respectively. The other physical parameters are shown in Table 2.

3.1.1. Oil film thickness analysis

The thickness field of the oil film can be represented as a plane in 3D space, and this plane can be defined by the thickness of three non-collinear points. In this paper, three points $A(R_2, 0)$, $B(R_2, \frac{2\pi}{3})$, and $C(R_2, \frac{4\pi}{3})$ on the simulation domain are taken to represent the thickness field of the oil film. Fig. 8 shows the physical locations of three points. The change in oil film thickness with angular displacement under typical operating conditions (20 MPa and 15,000 RPM) is shown in Fig. 9.

To avoid the influence of the initial state settings on the oil film state, the oil film state during the second cycle is used for analysis. It is worth noting that, in the second cycle, the inclination of the oil

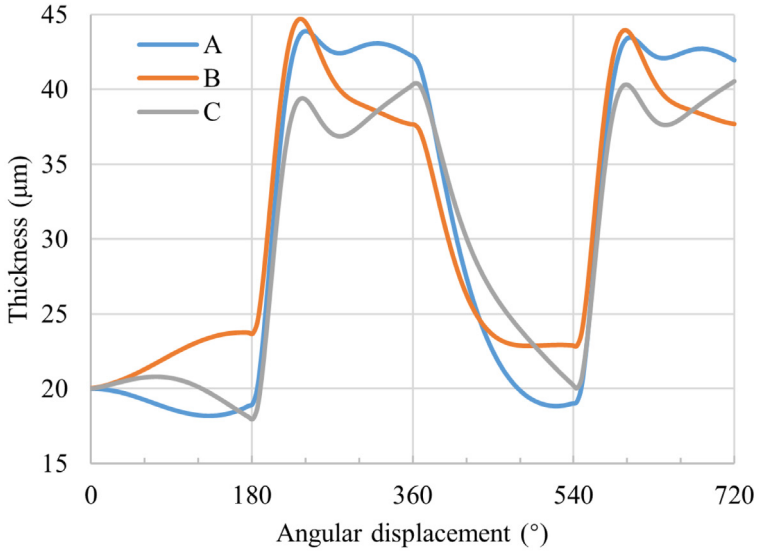

Fig. 9. Change curve of oil film thickness at three points (20 MPa and 15,000 RPM).

film in the low-pressure zone $(0°, 180°)$ is smaller than that in the high-pressure $(180°, 360°)$ zone. The difference in the inclination of the oil film between the high-pressure zone and the low-pressure zone is due to the different magnitudes of external loads acting on the oil film. Larger external loads require greater oil film support force to balance. A larger oil film inclination angle can provide more dynamic pressure support force, thereby offsetting more external loads from the plunger oil cavity pressure. This results in the oil film's inclination angle increasing as the external load increases.

Fig. 10 shows the variation of oil film thickness difference at different operating speeds in a 20 MPa working pressure. It can be seen that the higher operating speeds result in greater inertial forces, which exacerbate the oil film's tilt. This phenomenon reveals a complex balance between hydrodynamic and hydrostatic effects in the dynamic behavior of the slipper. At high speeds, the hydrodynamic wedge effect, generated by the slipper's tilt and rotation, becomes more pronounced, creating additional hydrodynamic load-bearing capacity. This is crucial for maintaining the necessary oil film thickness under high loads and preventing direct metal-to-metal contact. Therefore, the increase in the oil film's tilt angle can be viewed as an adaptive response of the system to cope with the increased dynamic loads.

3.1.2. Oil film pressure analysis

The throttling effect of the throttle hole causes a pressure drop. Notably, the inlet pressure is approximately linearly related to the working pressure and is minimally affected by the operating speed. This indicates that hydrostatic support is the primary load-bearing mechanism in this slipper design, especially in the high-pressure region. Hydrostatic pressure balance at the inlet is crucial for preventing slipper wear during startup and low-speed phases. Whether the PINN model can subsequently accurately capture this boundary condition, determined by the orifice and strongly correlated with the working pressure, is a key indicator of its physical consistency.

Fig. 11 shows the variation of inlet pressure with the angular displacement of the slipper under different working pressures and operating speeds. Fig. 11(a) illustrates the effect of varying rotational speeds, from 5,000 RPM to 25,000 RPM, while maintaining a constant working pressure of 20 MPa. The operating speed has been shown to have little effect on the inlet pressure. On the other hand, Fig. 11(b) shows that the working pressure has a dominant effect on the inlet pressure. At 15,000 RPM operating speed, the inlet pressure is approximately 90% of the working pressure, which is precisely due to the pressure drop caused by the throttling effect of the throttle hole.

Table 3
PINN hyperparameters.

Parameters	Value
Epoch	500
MLP size	5, 16, 64, 64, 16, 2
Learning rate	0.01, 0.001, 0.0001
Batch size	4096
Activation function	tanh
Data loss weight coefficient λ_1	1
Reynolds loss weight coefficient λ_2	1×10^{6}
Boundary conditions weight coefficient λ_3	1×10^{-12}
Continuity loss weight coefficient λ_4	1×10^{4}

3.2. Predictions of oil film from PINN

To apply the physics condition into the computational domain, a total of 11,250 collocation points are set at the inner and boundary of the oil film area, and the physics loss of the PINN models is computed at these collocation points. All these points are generated in uniformed distribution to ensure the convenience and stability of loss computation. Three levels of learning rate of the Adam optimizer are set at different stages of PINN training. A high learning rate is used for the first 25% epoch, a medium level of learning rate is used for 25% to 75% epoch, and a low learning rate is used after 75% to ensure the convergence of the total loss. The hyperparameters of PINN are shown in Table 3. In this study, the model is used as a full-loop surrogate with partial physics constraints. Specifically, lubrication physics (Reynolds, boundary, continuity, and geometric constraints) is enforced explicitly in the loss, while the influence of slipper dynamics is learned implicitly from labels generated by the coupled FDM simulation framework.

The convergence history of the PINN, depicted in Fig. 12, provides critical insight into the training dynamics and the successful integration of physical laws. The total loss for both the training and testing datasets exhibits a rapid and substantial decrease of over two orders of magnitude within the initial 100 epochs, before stabilizing to a low, converged value. Crucially, the nearly identical trajectories of the training and testing loss curves demonstrate the model's excellent generalization capability and the absence of overfitting, a key benefit derived from the regularization effect of the embedded physical constraints. A closer examination of the individual loss components reveals a distinct, hierarchical learning process. Initially, the training is dominated by the data loss, which plummets almost instantaneously

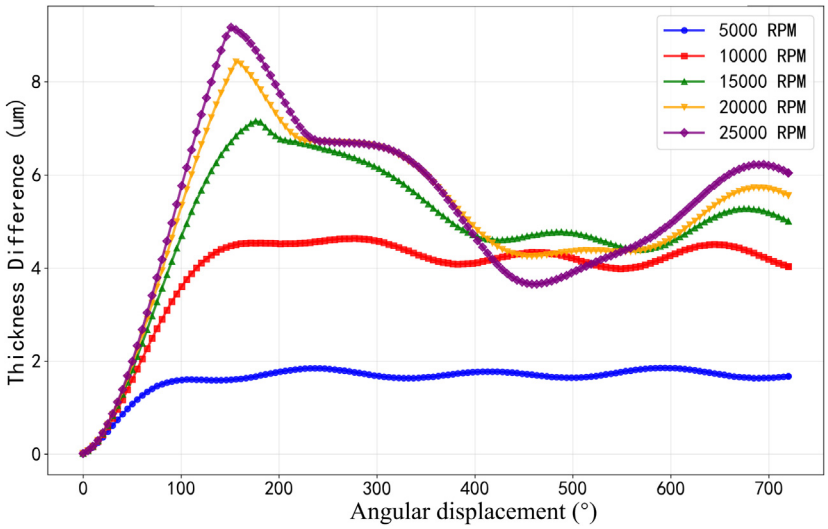

Fig. 10. Variation of thickness difference at different operating speed (20 Mpa).

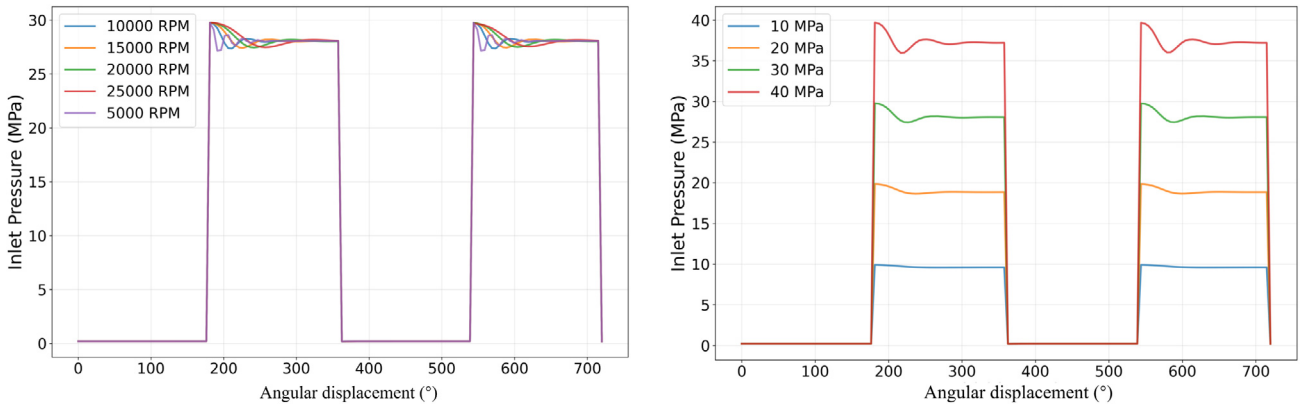

Fig. 11. Variation of inlet pressure in different working pressures and operating speeds.

as the network rapidly anchors its solution to the provided simulation data. Subsequently, as the data fidelity is achieved, the Reynolds equation loss becomes the primary contributor to the total loss and its steady reduction governs the refinement phase of the training. This transition signifies the core mechanism of the PINN, where the model shifts from a data-driven fitting exercise to a physics-constrained optimization, ensuring the solution is not only accurate at discrete points but also physically consistent across the entire computational domain. The eventual convergence of all loss components to a stable equilibrium confirms that the final model represents an optimal balance between data fidelity and adherence to the governing principles of fluid dynamics.

3.2.1. Transient results comparison

Fig. 13 shows the comparison of transient results produced by the proposed MLP Neural Network, PINN-1, PINN-2 and FDM in 30 MPa and 20,000 RPM. The results include the average oil film thickness, inlet pressure and average pressure. In this figure, Neural Networks refers to the PINN-1 model without any physical loss functions, i.e., a purely data-driven neural network. As this chart shows, the PINN model demonstrates higher accuracy in predicting oil film thickness compared to purely data-driven neural networks.

Purely data-driven neural network models exhibit significant limitations in predicting the transient dynamics of slipper pairs. Although the model can correctly identify the fundamental frequency periodicity of the system as the rotation angle changes, it tends to generate overly smoothed prediction curves due to data sparsity and a lack of physical inductive bias, thus losing crucial high-frequency dynamic details. As shown in the figure, the model fails to accurately reproduce the characteristic double-peak structure in the oil film thickness curve, exhibiting a smoothed sine waveform similar to a low-pass filter. Furthermore, in the pressure transient response, the model cannot capture the steep step changes in inlet pressure and mean pressure, resulting in significant hysteresis and waveform distortion during pressure build-up and unloading phases, and even predicting physically unreliable negative pressure values in the low-pressure region.

The PINN-1 model, incorporating soft constraints based on physical equations, significantly enhances its ability to capture nonlinear transient characteristics. Thanks to the guidance of the Reynolds equations and boundary conditions on the loss function, PINN-1 successfully reproduces most of the complex dynamics in FDM simulations, including rapid pressure rises and dramatic fluctuations in oil film thickness. However, due to the lack of strict geometric kinematic constraints, the model exhibits numerical instability in transitional regions with abrupt state changes (such as pressure abrupt changes near 180° and

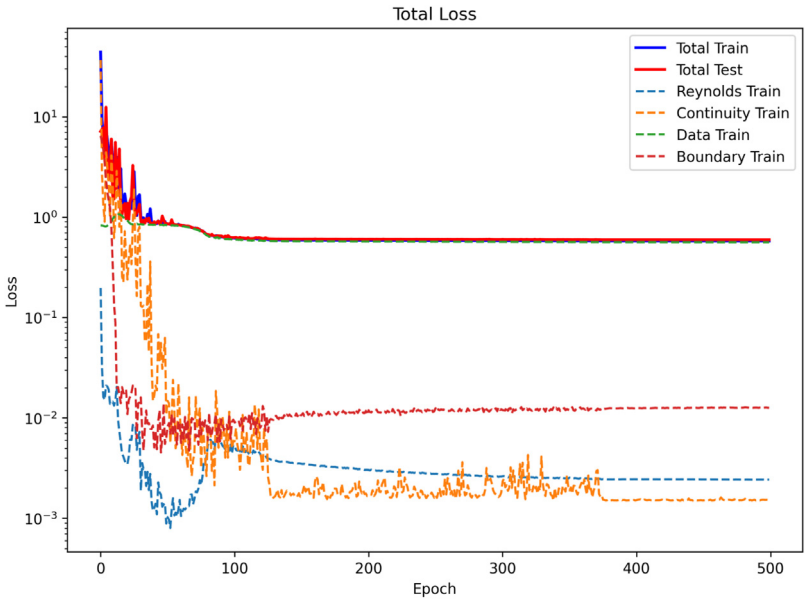

Fig. 12. Loss history of PINN training process.

360°). Obvious non-physical oscillations and overshoot are visible in the curves, indicating that relying solely on residual penalties from partial differential equations is insufficient to completely suppress local solution errors. This leads to convergence difficulties when handling high-gradient transient responses, failing to fully guarantee smoothness and physical consistency throughout the entire cycle. Furthermore, prediction accuracy decreased as the rotation angle approached 720°, highlighting a common challenge for machine learning models at the boundaries of training datasets: models excel in interpolation regions but may degrade in extrapolation or near the boundaries.

The PINN-2 model, employing hard geometric constraints, demonstrates superior transient accuracy and robustness, with its prediction curve achieving near-perfect agreement with the FDM benchmark solution. By explicitly embedding the rigid-body kinematics of the slipper into the network architecture, PINN-2 eliminates the oscillations present in PINN-1, ensuring a smooth transition between oil film thickness and pressure changes. This model not only accurately captures minute peak-to-valley variations in oil film thickness but also exhibits extremely high rigidity in the step response of the pressure field, capable of reproducing the instantaneous pressure build-up and unloading with almost no time delay or overshoot. This high degree of agreement confirms that combining physical conservation laws with hard geometric constraints can effectively overcome the smoothing effect of purely data-driven methods and the numerical jitter of soft-constraint methods, thereby achieving high-fidelity transient prediction of complex tribodynamic systems.

3.2.2. Field results comparison

Fig. 14 shows a comparison of the pressure field produced by the MLP neural network, PINN-1, PINN-2, and FDM at $\phi = 270°$ under working conditions of 30 MPa and 20,000 RPM, which are not included in the training set. The FDM simulation results are treated as an approximate theoretical solution. The difference between the theoretical solutions and the predicted results can be used to obtain the error in the pressure field and the error in the thickness field.

While the purely data-driven neural network model can capture the overall trend of pressure decreasing from the inner radial to the outer radial direction on a macroscopic scale, they exhibit significant limitations in quantitative accuracy. As shown in Fig. 14, the error distribution of this model presents a distinct concentric circle region of high amplitude, with a peak error approaching 2.6 MPa, a mean absolute error (MAE) as high as 2.36 MPa, and a relative error of 8.0%. This systematic bias indicates that, in the absence of constraints from physical laws such as the Reynolds equation, relying solely on data fitting is insufficient to accurately reproduce the complex gradient characteristics in fluid dynamics, especially in regions of rapid pressure changes, where the model cannot guarantee physical consistency.

The PINN-1 model significantly improves the prediction fidelity of the pressure field by embedding the Reynolds equation into the loss function, demonstrating the effectiveness of physical information in the output of the gauge network. Compared with the purely data-driven model, the error distribution of PINN-1 is significantly reduced, with the mean absolute error decreasing to 0.89 MPa, indicating that the introduction of the governing equation successfully guides the model to learn the correct fluid dynamics behavior. However, residual annular error distributions are still visible in the error contour plot, suggesting that relying solely on the soft constraint form of the partial differential equations is insufficient to eliminate the uncertainties of numerical calculations in certain local regions, leaving room for improvement in the uniformity of the pressure distribution in the circumferential direction.

The PINN-2 model, employing an improved architecture, demonstrates superior pressure prediction performance, achieving a high degree of agreement with numerical simulation benchmarks. Error analysis reveals that the PINN-2 error field is virtually blank, indicating that its predicted values are extremely close to the true values across the entire computational domain. The mean absolute error is further reduced to 0.45 MPa, with a maximum relative error of only 1.9%. This outstanding performance confirms that the enhanced constraint mechanism effectively eliminates non-physical fluctuations in the pressure field, enabling the model to not only surpass the previous two methods in numerical accuracy but also to reproduce complex fluid pressure gradient distributions with exceptional precision, achieving a perfect capture of high-fidelity flow field characteristics.

Fig. 15 shows the comparison of thickness field produced by MLP neural network, PINN-1, PINN-2 and FDM at $\phi = 270°$ when working conditions are 30 MPa and 20,000 RPM. Purely data-driven neural network models exhibit a severe lack of physical consistency in predicting the thickness of the skid's underside oil film. Although the model attempts to establish a mapping between input and output through extensive data fitting, the lack of rigid body kinematic constraints results in significant non-physical nonlinear distortions in the predicted

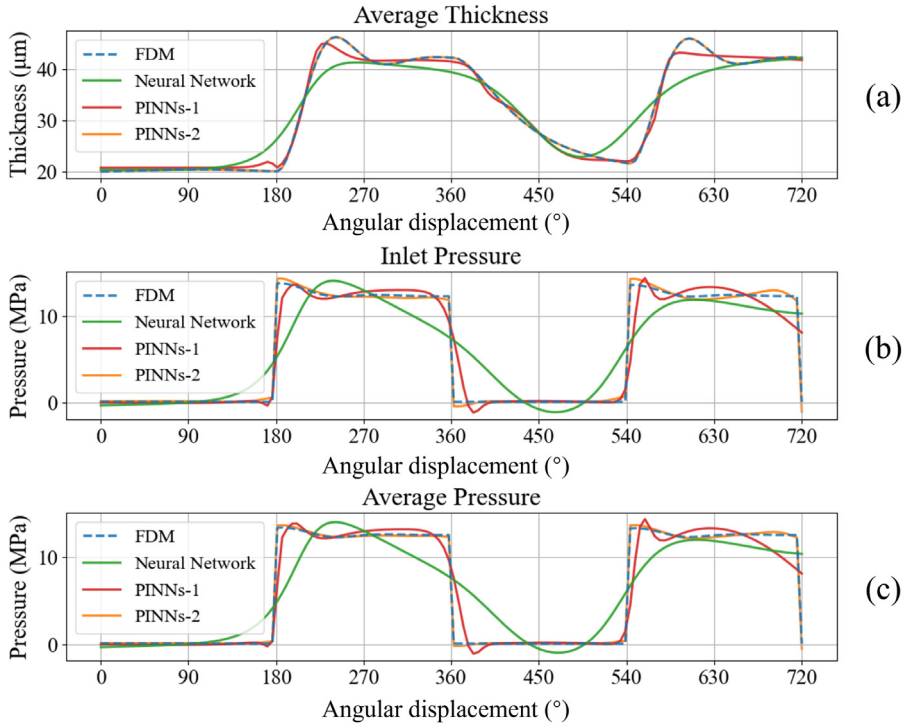

Fig. 13. Comparison of transient results produced by proposed MLP Neural Network, PINN-1, PINN-2 and FDM (30 MPa and 20,000 RPM):(a) Average Thickness (b) Inlet Pressure (c) Average Pressure.

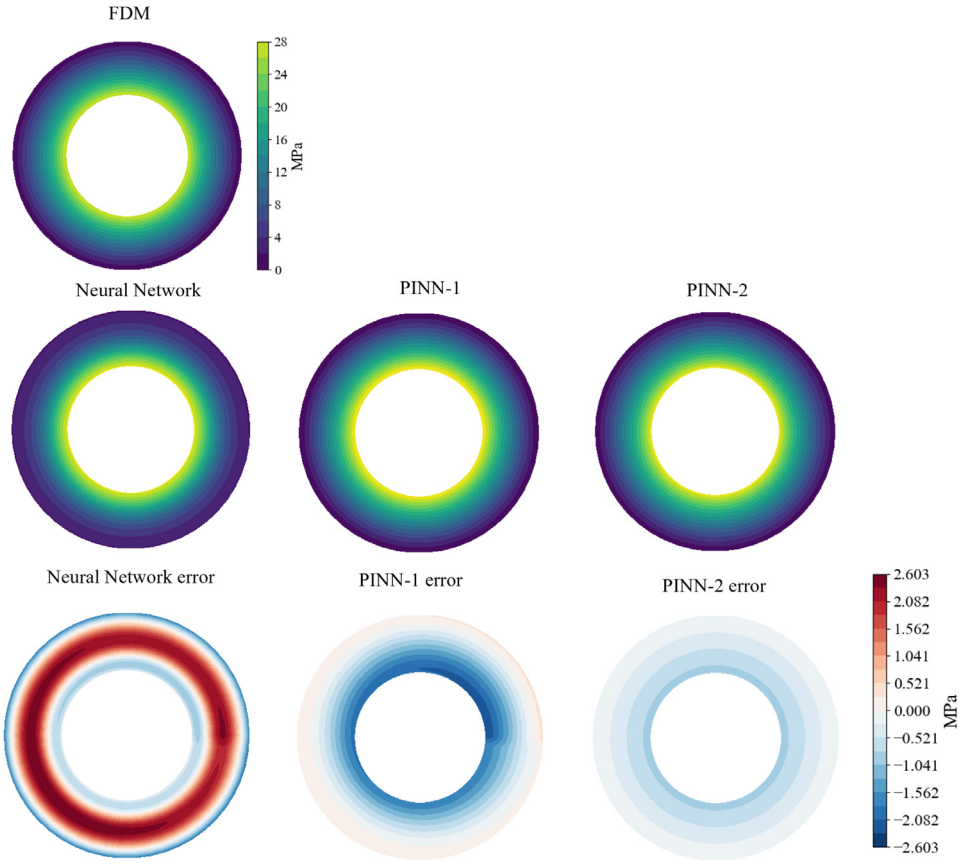

Fig. 14. Comparison of the pressure distribution produced by proposed MLP Neural Network, PINN-1, PINN-2 and FDM (30 MPa, 20,000 RPM and 270 °).

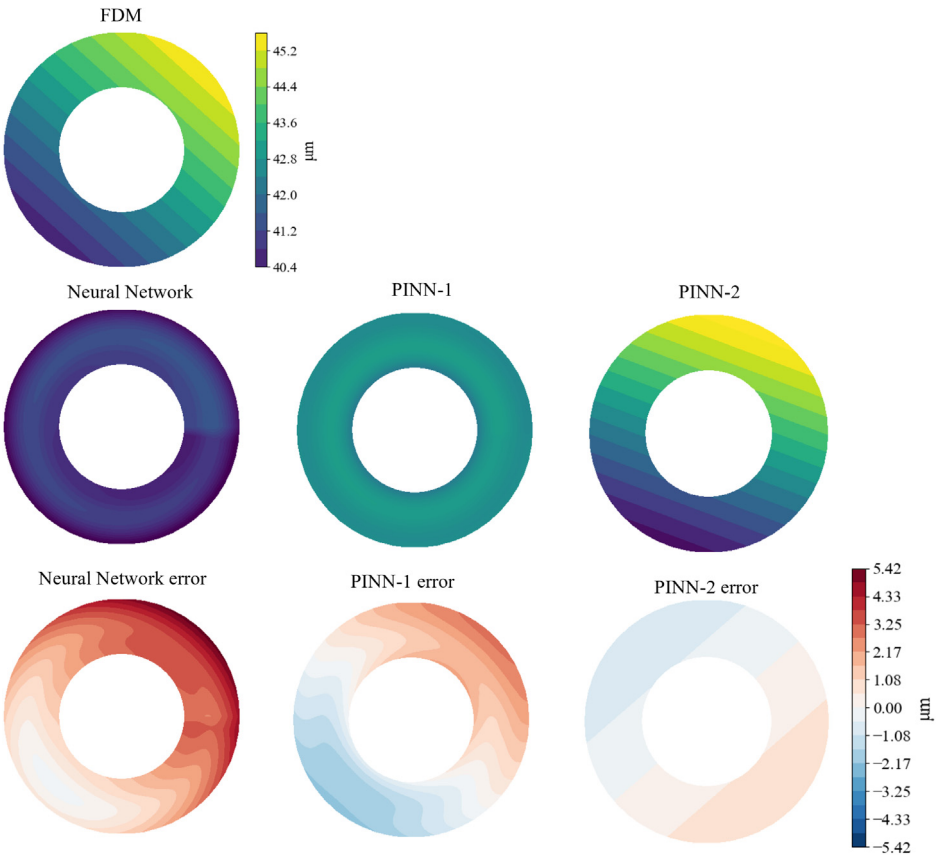

Fig. 15. Comparison of the thickness distribution produced by proposed MLP Neural Network, PINN-1, PINN-2 and FDM (30 MPa, 20,000 RPM and 270 °).

thickness field, failing to reproduce the planar characteristics expected when the skid is tilted. As shown in the figure, the error distribution contour plot reveals extremely high deviation regions, and the thickness distribution exhibits a curved ring-shaped topology with a high center and low sides, severely violating the physical fact that the slipper's bottom surface is a rigid plane. Theoretically, the oil film thickness should adhere to the geometric relationship described in Eq. (5), meaning it should be a flat surface at all times. Quantitative results further confirm this, with the model's mean absolute error (MAE) reaching 2.4 μ m and a relative error of 8.0%, indicating that relying solely on data-driven methods is insufficient to accurately generalize the complex motion postures of skids in the absence of geometric prior knowledge.

While the PINN-1 model incorporates the Reynolds equation as a physical soft constraint, it has not achieved a qualitative breakthrough in the geometric reconstruction of the thickness field. Although the inclusion of the physical equation constrains the flow field variables to some extent, the thickness h still participates in training as a free output field of the network. The network tends to minimize the Reynolds equation residuals by locally adjusting the thickness values, rather than learning global geometric laws. This results in the PINN-1 model predicting a thickness distribution with a lower numerical error than pure neural networks (MAE reduced to 1.44 μm), but its error contour plot still shows a significant wavy distribution, indicating that the predicted surface still exhibits non-physical warping deformations. This geometric inconsistency reveals the limitations of soft constraint mechanisms in handling problems with strong geometric dependencies; that is, relying solely on PDE residuals is insufficient to force the network to adhere to strict geometric constraints.

The PINN-2 model, which incorporates hard geometric constraints, completely solves the physical consistency problem of thickness prediction and achieves high-fidelity reproduction of FDM simulation results. By reconstructing the network output layer, the original spatial thickness field prediction is transformed into the prediction of three monitoring points(h_1, h_2, h_3). PINN-2 mathematically enforces that the output oil film thickness always satisfies the plane equation constraints. This improvement ensures that the prediction results perfectly match the actual physical plane in terms of geometry, eliminating the nonlinear distortions that appeared in the previous two models. Reflected in the error contour plot, the deviation of PINN-2 is almost negligible, with its mean absolute error significantly reduced to 0.53 μm and its relative error to only 1.7%, strongly demonstrating that explicitly embedding hard geometric kinematic constraints is a key strategy to ensure the physical interpretability and accuracy of the tribological surrogate model.

The error metrics for the prediction accuracy of the PINN model with different constrain are presented in Table 4. In these metrics, three indicators are used to evaluate errors of results, namely (i) the mean absolute error (MAE), (ii) relative error (RE) and (iii) the maximum relative error (REmax). MAE is used to measure the average deviation between predicted values and FDM reference values, and is defined in Eq. (18) as follows:

$$MAE = \frac{1}{N_d}\sum_{i=1}^{N_d}|\hat{y}_i - y_i|, \tag{18}$$

where N_d represents the total number of sample points in the test set, $\hat{y}_i$ is the model predicted value (pressure p or thickness h), and y_i is the corresponding FDM simulation true value.

For the oil film thickness field, since its value is always greater than zero throughout the entire domain, the mean relative error (RE) defined in Eq. (19) was used to evaluate its prediction accuracy:

$$RE = \frac{1}{N_d}\sum_{i=1}^{N_d}\left|\frac{\hat{y}_i - y_i}{y_i}\right| \times 100\% \tag{19}$$

For the pressure field, considering that the outlet pressure at the outer diameter of the slipper is close to 0, directly calculating the

Table 4
Error metrics comparison between FDM simulation and PINN prediction (30 MPa, 20000 RPM)

Methods	Pressure		Thickness	
	MAE (MPa)	REmax	MAE (μ m)	RE
Pure data	2.36	3.8%	2.4	8.0%
PINN-1	0.89	3.2%	1.44	4.8%
PINN-2	0.45	1.9%	0.53	1.7%

point-by-point relative error would cause the denominator to approach zero, resulting in significant numerical instability. Therefore, to more robustly assess the relative deviation of the pressure field, this paper introduces the maximum relative error (RE_{max}), which is defined in Eq. (20) as the ratio of the maximum absolute error to the maximum value in the reference range (i.e., the L_∞ norm relative error):

$$RE_{max} = \frac{\max|\hat{y}_i - y_i|}{\max|y_i|} \times 100\% \tag{20}$$

This metric (RE_{max}) can effectively avoid numerical singularities in low-pressure areas, while intuitively reflecting the relative accuracy of the model in capturing maximum pressure characteristics.

3.2.3. Uncertainty and randomness analysis

To evaluate the robustness of the proposed model with respect to stochastic training effects, five independent training runs were conducted under identical hyperparameters but different random initializations and data shuffling orders. The predictive variability was assessed using the central film thickness h_c under the unseen test operating condition.

Fig. 16 illustrates the mean prediction together with the $\pm1\sigma$ and $\pm2\sigma$ confidence bands obtained from the five runs. The results demonstrate an excellent repeatability of the model. The five individual realizations almost completely overlap with the mean curve throughout the entire operating cycle. The uncertainty bands remain extremely narrow, even in regions characterized by rapid thickness transitions and high gradients (around 200° and 600°), where numerical instability would typically be more likely to occur. Quantitatively, the maximum deviation across runs is negligible compared to the absolute magnitude of the film thickness, and the fluctuation amplitude remains well within the $\pm2\sigma$ envelope across the full rotational range. This indicates that the model converges consistently toward a stable solution manifold, and the embedded physical constraints effectively regularize the optimization process, preventing divergence to alternative local minima. These results confirm that the proposed framework exhibits strong training stability and low sensitivity to random initialization, ensuring that the reported predictive performance is reproducible and not dependent on a particular stochastic realization.

3.2.4. Generalization sensitivity to training points distance

To verify the generalization ability of the PINN model, we conducted a sensitivity analysis based on intra-domain distance under different operating conditions. The analysis is conducted in the $(P_{\text{work}}, \omega)$ space, where P_{work} is working pressure and ω is rotational speed in RPM. For each test condition, the normalized nearest-training-point distance is defined as:

$$d = \min_{(P_j,\omega_j)\in D_{\text{train}}} \sqrt{\left(\frac{P_{\text{work}} - P_j}{10\ \text{MPa}}\right)^2 + \left(\frac{\omega - \omega_j}{5{,}000\ \text{RPM}}\right)^2}. \tag{21}$$

Notably, the denominator 10 MPa and 5,000 RPM are the pressure/speed intervals used in dataset construction, ensuring a dimensionless and scale-consistent distance measure. Three representative in-domain conditions were selected to form Near/ Medium/ Far levels of data support, namely (i) Near: (20 MPa, 11,250 RPM); (ii) Medium: (25 MPa, 12,500 RPM); (iii) Far: (20 MPa, 15,000 RPM); with the corresponding dimensionless distances $d = 0.250,\ 0.707,\ 1.000$, respectively.

Table 5
Transposed error metrics of PINN-2 for near/medium/far in-domain cases.

Metric	Near	Medium	Far
Pressure MAE (MPa)	0.24	0.38	0.45
Pressure $RE_{\max}$ (%)	1.0	1.6	1.9
Thickness MAE (μm)	0.33	0.47	0.53
Thickness RE (%)	0.9	1.1	1.7

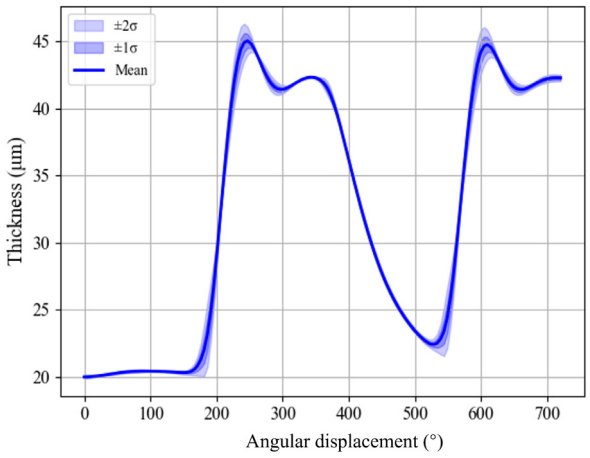

Fig. 16. Uncertainty quantification of predicted central film thickness h_c over five independent training runs (mean curve with $\pm1\sigma$ and $\pm2\sigma$ bands).

For each case, we evaluate pressure-field errors using MAE and $RE_{\max}$, and thickness-field errors using MAE and RE. The transposed summary is listed in Table 5. As d increases from Near to Far, all error metrics increase monotonically, indicating a clear distance-sensitive trend. This confirms that prediction quality is highest near well-supported training regions and degrades gradually as the condition moves farther from the training set, even within the original operating envelope. Importantly, the observed degradation remains controlled, and PINN-2 preserves physically consistent predictions across all three in-domain cases. These results support the robustness of the proposed hard-constrained framework for practical operating-condition variation.

3.2.5. Computational efficiency

Table 6 summarizes the computational cost of the FDM simulation and the neural-network-based models. The reported preparation time for 22 scenarios is 14,938 s, which corresponds to the one-time offline cost of generating the full FDM dataset used for model development and evaluation. For model training, the pure data-driven Neural Network (NN) requires 271 s, while PINN-1 and PINN-2 require 528 s and 595 s, respectively. The additional training cost of PINN models is expected, since physics-based constraints introduce extra computational overhead during optimization.

For online prediction, FDM requires 679 s to complete one operating cycle, whereas all trained neural-network-based models complete the same prediction in 2 s. This indicates an inference-time reduction of approximately 99.7% relative to FDM. Overall, although offline data preparation and PINN training are more expensive, these costs are incurred only once; the resulting surrogate models provide substantial acceleration for repeated evaluations, making them suitable for rapid parametric studies and near real-time applications.

4. Conclusion and outlook

This study has successfully established and validated a physics-informed machine learning framework for the rapid prediction of lubrication characteristics in axial piston pump slipper pairs. The proposed

Table 6
Comparison of run time between FDM simulation and PINN prediction.

Methods	FDM simulation	Neural Network	PINN-1	PINN-2
Simulation time of 22 scenarios (s)	14,938	–	–	–
Training time (s)	–	271	528	595
Run time (s)	679	2	2	2

model, by embedding the Reynolds equation and mass continuity directly into the loss function, achieved a computational speedup of approximately 99.7% compared to the traditional Finite Difference Methods (FDM), reducing the simulation time from 679 s to just 2 s per cycle while maintaining high accuracy compared to high-fidelity numerical simulation results. A critical comparative analysis revealed the limitations of standard soft-constrained formulations (PINN-1), which, despite capturing general transient trends, suffered from geometric inconsistencies in film thickness distribution with a relative error of 4.8%. In contrast, the enhanced architecture (PINN-2) incorporating explicit hard geometric constraints significantly improved physical fidelity, reducing the thickness relative error to 1.7% and the pressure mean absolute error to 0.45 MPa. These results conclusively demonstrate that ensuring the physical validity of data-driven tribological models requires explicit inclusion of lubrication-governing equations and strict kinematic constraints, but also the strict enforcement of kinematic constraints to guarantee robust and interpretable solutions.

Although the proposed PINN-2 framework demonstrates strong accuracy and efficiency within the investigated operating envelope, several potential underperformance scenarios should be acknowledged. Prediction accuracy may degrade when the model is applied to operating conditions with limited representation in the training set, particularly in regions with rapid transient changes and steep pressure/thickness gradients. In addition, because the current formulation is built on the present Reynolds-based framework and prescribed constraints, its reliability may be reduced in regimes dominated by coupled physics that are not explicitly modeled, such as strong thermo-elastohydrodynamic effects, severe cavitation, or roughness-driven mixed lubrication. Therefore, the present model should be interpreted as a high-fidelity surrogate within its validated physical and data domain, and not yet as a universal solver for all lubrication regimes.

Building upon the findings of this study, future research will aim to extend this efficient surrogate modeling approach to encompass a fully coupled, multi-degree-of-freedom dynamic system where the PINN serves as an embedded solver for real-time kinematic interactions. A key next step is to explicitly incorporate the slipper dynamic equilibrium equation into the training objective as an additional physics residual. The scope of physical modeling should be broadened to include thermal-elastohydrodynamic lubrication (TEHL) effects, surface roughness in mixed lubrication regimes, and cavitation phenomena to enhance applicability under extreme operating conditions. Additionally, investigations into advanced neural network architectures, such as those employing adaptive activation functions or curriculum learning, will be prioritized to further optimize convergence and stability. Ultimately, the superior computational efficiency demonstrated by the PINN-2 model paves the way for its integration into digital twin frameworks, enabling real-time health monitoring, fault diagnosis, and operational optimization of hydraulic machinery.

CRediT authorship contribution statement

Hongsen Qiu: Writing – review & editing, Writing – original draft, Visualization, Validation, Software, Methodology, Investigation, Formal analysis, Data curation, Conceptualization. **Lawrence Tinsley:** Writing – review & editing, Supervision. **Agusmian Partogi Ompusunggu:** Writing – review & editing, Supervision, Resources, Project administration, Methodology, Conceptualization.

Declaration of Generative AI and AI-assisted technologies in the writing process

During the preparation of this work, the authors used [Gemini] in order to [Rewrite/rephrase sentences]. After using this tool/service, the authors reviewed and edited the content as needed and take full responsibility for the content of the published article.

Declaration of competing interest

The authors declare that they have no known competing financial interests or personal relationships that could have appeared to influence the work reported in this paper.

Appendix. Derivation

A.1. Derivation of the axial piston force component (F_z)

The axial force component F_z is the projection of the hydraulic load from the piston chamber onto the slipper's central axis z_s, see Fig. 3. The primary hydraulic force acting on the piston end is determined by the product of the instantaneous working pressure p_w and the piston cross-sectional area $A_p = \pi R_p^2$, resulting in a total magnitude of $F_{piston} = p_w \pi R_p^2$. Due to the geometric configuration of the swashplate mechanism, the slipper's central axis is inclined by an angle β relative to the piston's translational axis. Consequently, the force transmitted through the spherical joint must be projected onto the slipper's local coordinate system by multiplying by $\cos\beta$. Since the positive z_s direction is defined as pointing away from the swashplate (increasing film thickness), this compressive hydraulic load acts in the negative direction, leading to the derived expression $F_z = -\pi R_p^2 p_w \cos\beta$.

A.2. Derivation of the oil film thickness equation

The local oil film thickness $h(r,\theta,t)$ is geometrically defined by the rigid body kinematics of the slipper sealing land moving relative to the swashplate surface. By establishing a local Cartesian coordinate system fixed to the slipper center, the clearance height for a tilted planar surface can be linearly expressed as $h(x,y,t) = h_c(t) + \lambda_y y + \lambda_x x$, where $h_c(t)$ represents the central film thickness and the coefficients λ_y, λ_x correspond to the planar slopes. Introducing the slipper's generalized coordinates where $\alpha(t)$ and $\beta(t)$ denote the tilting angles inducing height variations along the y-axis and x-axis respectively, and substituting the polar coordinate transformations $x = r\cos\theta$ and $y = r\sin\theta$, the equation yields the final kinematic relationship $h(r,\theta,t) = h_c(t) + \alpha(t) r\sin\theta + \beta(t) r\cos\theta$. This derivation assumes small angle approximations which are valid given the micron-scale magnitude of the lubrication gap.

Data availability

Data will be made available on request.

References

[1] Guo S, Chen J, Lu Y, Wang Y, Dong H. Hydraulic piston pump in civil aircraft: Current status, future directions and critical technologies. Chin J Aeronaut 2020;33(1):16–30. http://dx.doi.org/10.1016/j.cja.2019.01.013, URL https://www.sciencedirect.com/science/article/pii/S1000936119300615.

[2] Zhang J, Chao Q, Xu B. Analysis of the cylinder block tilting inertia moment and its effect on the performance of high-speed electro-hydrostatic actuator pumps of aircraft. Chin J Aeronaut 2018;31(1):169–77. http://dx.doi.org/10.1016/j.cja.2017.02.010, URL https://www.sciencedirect.com/science/article/pii/S1000936117300298.

[3] Ma Z, Wang S, Shi J, Li T, Wang X. Fault diagnosis of an intelligent hydraulic pump based on a nonlinear unknown input observer. Chin J Aeronaut 2018;31(2):385–94. http://dx.doi.org/10.1016/j.cja.2017.05.004, URL https://www.sciencedirect.com/science/article/pii/S1000936117301085.

[4] Hashemi S, Friedrich H, Bobach L, Bartel D. Validation of a thermal elasto-hydrodynamic multibody dynamics model of the slipper pad by friction force measurement in the axial piston pump. Tribol Int 2017;115:319–37. http://dx.doi.org/10.1016/j.triboint.2017.05.013, URL https://www.sciencedirect.com/science/article/pii/S0301679X17302396.

[5] Wang H, Shi G. Lubrication characteristics of the worn slipper in the slipper-swashplate pair. Ind Lubr Tribol 2021;73(7):1037–44. http://dx.doi.org/10.1108/ILT-07-2021-0241, URL https://www.emerald.com/insight/content/doi/10.1108/ilt-07-2021-0241/full/html, Publisher: Emerald Publishing Limited.

[6] Liu S, Li Z, Sun W, Ai C, Zhang W, Zhang Y, Chen Z. A mixed lubrication model for predicting the Lubrication performance degradation behavior of slipper pair in early wear failure. IEEE Access 2023;11:100479–94. http://dx.doi.org/10.1109/ACCESS.2023.3315124, URL https://ieeexplore.ieee.org/abstract/document/10250793.

[7] Wang H, Lin N, Yuan S, Liu Z, Yu Y, Zeng Q, Fan J, Li D, Wu Y. Structural improvement, material selection and surface treatment for improved tribological performance of friction pairs in axial piston pumps: A review. Tribol Int 2024;198:109838. http://dx.doi.org/10.1016/j.triboint.2024.109838, URL https://www.sciencedirect.com/science/article/pii/S0301679X24005905.

[8] Raissi M, Perdikaris P, Karniadakis GE. Physics-informed neural networks: A deep learning framework for solving forward and inverse problems involving nonlinear partial differential equations. J Comput Phys 2019;378:686–707. http://dx.doi.org/10.1016/j.jcp.2018.10.045, URL https://www.sciencedirect.com/science/article/pii/S0021999118307125.

[9] Lyu F, Zhang J, Sun G, Xu B, Pan M, Huang X, Xu H. Research on wear prediction of piston/cylinder pair in axial piston pumps. Wear 2020;456–457:203338. http://dx.doi.org/10.1016/j.wear.2020.203338, URL https://www.sciencedirect.com/science/article/pii/S0043164820302775.

[10] Cuomo S, Di Cola VS, Giampaolo F, Rozza G, Raissi M, Piccialli F. Scientific machine learning through physics–informed neural networks: Where we are and What's Next. J Sci Comput 2022;92(3):88. http://dx.doi.org/10.1007/s10915-022-01939-z.

[11] Rahman JU, Nimra. DiffGrad for physics-informed neural networks. 2024, http://dx.doi.org/10.48550/arXiv.2409.03239, URL http://arxiv.org/abs/2409.03239arXiv:2409.03239[cs].

[12] Sekhar J, Reva A, Sekhar J. Embedding physics into deep learning: A structured review of physics-informed neural networks. 2025, http://dx.doi.org/10.20944/preprints202504.2577.v1, URL https://www.preprints.org/manuscript/202504.2577/v1.

[13] Zhao C, Zhang F, Lou W, Wang X, Yang J. A comprehensive review of advances in physics-informed neural networks and their applications in complex fluid dynamics. Phys Fluids 2024;36(10):101301. http://dx.doi.org/10.1063/5.0226562.

[14] Toscano JD, Oommen V, Varghese AJ, Zou Z, Ahmadi Daryakenari N, Wu C, Karniadakis GE. From PINNs to PIKANs: recent advances in physics-informed machine learning. Mach Learn Comput Sci Eng 2025;1(1):15. http://dx.doi.org/10.1007/s44379-025-00015-1.

[15] Zhu Z, Zhao Y, Ompusunggu AP. Physics-informed machine learning for near real-time stress prediction on a structural component: Application for landing gears. Eng Appl Artif Intell 2025;162:112532. http://dx.doi.org/10.1016/j.engappai.2025.112532, URL https://www.sciencedirect.com/science/article/pii/S0952197625025631.

[16] Almqvist A. Fundamentals of physics-informed neural networks applied to solve the Reynolds boundary value problem. Lubricants 2021;9(8):82. http://dx.doi.org/10.3390/lubricants9080082, URL https://www.mdpi.com/2075-4442/9/8/82, Number: 8 Publisher: Multidisciplinary Digital Publishing Institute.

[17] Zhao K, He T, Wang C, Chen Q, Li Z. Lubrication characteristics analysis of slipper pair of digital valve distribution axial piston pump. Adv Mech Eng 2022;14(3). http://dx.doi.org/10.1177/16878132221085442, URL https://www.scopus.com/inward/record.uri?eid=2-s2.0-85126669430&doi=10.1177%2f16878132221085442&partnerID=40&md5=c9279125d162169ce2e6648da48ad9d3.

[18] Li L, Li Y, Du Q, Liu T, Xie Y. ReF-nets: Physics-informed neural network for Reynolds equation of gas bearing. Comput Methods Appl Mech Engrg 2022;391:114524. http://dx.doi.org/10.1016/j.cma.2021.114524, URL https://www.sciencedirect.com/science/article/pii/S0045782521007180.

[19] Xi Y, Deng J, Li Y. A solution for finite journal bearings by using physics-informed neural networks with both soft and hard constrains. Ind Lubr Tribol 2023;75(5):560–7. http://dx.doi.org/10.1108/ILT-02-2023-0045, URL https://www.proquest.com/docview/2829390428/abstract/411FDD4018304CDFPQ/1, Num Pages: 8 Publisher: Emerald Group Publishing Limited.

[20] Rom M. Physics-informed neural networks for the Reynolds equation with cavitation modeling. Tribol Int 2023;179:108141. http://dx.doi.org/10.1016/j.triboint.2022.108141, URL https://www.sciencedirect.com/science/article/pii/S0301679X22007125.

[21] Cheng Y, He Q, Huang W, Liu Y, Li Y, Li D. HL-nets: Physics-informed neural networks for hydrodynamic lubrication with cavitation. Tribol Int 2023;188. http://dx.doi.org/10.1016/j.triboint.2023.108871, URL https://www.scopus.com/inward/record.uri?eid=2-s2.0-85168835259&doi=10.1016%2fj.triboint.2023.108871&partnerID=40&md5=801cb5c113e1ee10ae010066fce8ec01.

[22] Huang B, Bao F, Wei C, Luo Z. Design of slipper pair based on oil film dynamic lubrication mechanism, vol. 105, 2021, p. 135–46. http://dx.doi.org/10.1007/978-3-030-75793-9_14, URL https://www.scopus.com/inward/record.uri?eid=2-s2.0-85106019911&doi=10.1007%2f978-3-030-75793-9_14&partnerID=40&md5=f75e660dbb0f2500af0b4deababe86a8.

[23] Ransegnola T, Shang L, Vacca A. A study of piston and slipper spin in swashplate type axial piston machines. Tribol Int 2022;167:107420. http://dx.doi.org/10.1016/j.triboint.2021.107420, URL https://www.sciencedirect.com/science/article/pii/S0301679X21005685.

[24] Du Z, Zhang Y, Lu W, Huang W. Research on prediction methods for eccentric wear of the slipper pair in axial piston pumps and lubrication performance analysis. J Tribol 2024;146(9). http://dx.doi.org/10.1115/1.4065266, URL https://www.scopus.com/inward/record.uri?eid=2-s2.0-85192675678&doi=10.1115%2f1.4065266&partnerID=40&md5=e51865b7c39a326fd39bd21f848fced3.

[25] Zhao K, He T, Wang C, Luo G, Zheng H. Study on fluid dynamic lubrication numerical analysis and surface topography design of slipper pair of valve distribution piston pump. Phys Fluids 2024;36(9). http://dx.doi.org/10.1063/5.0223252, URL https://www.scopus.com/inward/record.uri?eid=2-s2.0-85205982165&doi=10.1063%2f5.0223252&partnerID=40&md5=669cce706f5fbf2997447454488842b9.

[26] Ye S, Sun Y, Zhang J, Chen J, Xu B, Zhao S, Liu H. A new coupled dynamic model to study the vibration and lubrication characteristics of slipper/swash-plate interface in an axial piston pump. Proc Inst Mech Eng Part J: J Eng Tribol 2025;13506501241308942. http://dx.doi.org/10.1177/13506501241308942, Publisher: IMECHE.

[27] Dowson D. A generalized Reynolds equation for fluid-film lubrication. Int J Mech Sci 1962;4(2):159–70.

[28] Young DM. Iterative solution of large linear systems. Elsevier; 2014.

[29] Cybenko G. Approximation by superpositions of a sigmoidal function. Math Control Signals Systems 1989;2(4):303–14.

[30] LeCun Y, Bottou L, Orr GB, Müller K-R. Efficient backprop. In: Neural networks: tricks of the trade. Springer; 2002, p. 9–50.

DSPACE

https://dspace.org/

Lubrication film thickness prediction in the sliding contacts of axial piston pumps using physics-informed neural network

Qiu, Hongsen; Tinsley, Lawrence; Ompusunggu, Agusmian Partogi

2026-09
Elsevier
https://doi.org/10.1016/j.triboint.2026.112049
Qiu H, Tinsley L, Ompusunggu AP. (2026) Lubrication film thickness prediction in the sliding contacts of axial piston pumps using physics-informed neural network. Tribology International, Volume 221, September 2026, Article number 112049

Downloaded from a DSpace repository. https://dspace.org/